International Journal of Impact Engineering 182 (2023) 104764

Contents lists available at ScienceDirect

International Journal of Impact Engineering

journal homepage: www.elsevier.com/locate/ijimpeng

An automatic thermo-mechanical testing apparatus for metal forming applications

Julen Agirre [a], David Abedul [a], Eneko Saenz de Argandoña [a], Nagore Otegi [a], Lander Galdos [a], Borja Erice [a,b,*]

[a] Mondragon Unibertsitatea, Faculty of Engineering, Department of Mechanics and Industrial Production, Loramendi 4, Mondragon 20500, Gipuzkoa, Spain
[b] IKERBASQUE, Basque Foundation for Science, Bilbao, Spain

ARTICLE INFO

Keywords:
Metal forming
Intermediate strain rate, Hopkinson bar
High temperature
Experimental techniques

ABSTRACT

Dynamic testing of materials is necessary to model high-speed forming processes (e.g. hammer forging, blanking, forming, etc.) and crash/impact behaviour of structures, amongst others. The most common machines to perform medium to high-speed tests are the servo-hydraulic high-speed tensile and compression machines and the Hopkinson bars. The paper analyses the use of a newly-developed laboratory testing facility, named the Automatic Thermo-Mechanical Tester (ATMT). This testing machine is equipped with a pneumatically accelerated Direct Impact Drop Hammer (DIDH), a furnace and automatised robotic arm, capable of characterising materials at intermediate strain rates, ranging from 100 to 300 s^{-1} in combination with temperatures up to 1350 °C. The hammer has been designed and constructed to conduct a variety of material characterisation tests, such as, upsetting or plane strain compression tests as well as component tests for validation purposes. The DIDH allows testing standard compression specimens at average strain rates in the order of 100 s^{-1} that decrease progressively until the it is fully stopped. It is, in combination with universal testing machines and Hopkinson bar systems, particularly suitable for experimental validation of loading-rate dependant material models. Compression tests were conducted with different hammer impact velocities generating a variety of strain rates at varying temperatures on S235JR structural steel, OFHC copper and wrought Inconel 625 nickel-based superalloy to assess the potential of the novel apparatus. A detailed finite element numerical study of the system was performed to assess several aspects such as the effect of the specimen geometry or its capability as an intermediate testing device, simulating a simplified system and the full Direct Impact Drop Hammer apparatus.

1. Introduction

The study of the mechanical behaviour of metals at different strains, strain rates and temperatures are essential because of the influence of these on critical metal forming process parameters. Some of these include the forming forces and ductility of the material at the macroscopic level as pointed out by [35,45], or recrystallization phenomena, at the microscopic level, see [36] or [46], for example. It is already well established that the strain rate and temperature at which metals are processed have a direct effect on the resulting mechanical properties, thus impacting on the performance of the final manufactured component as described by [9].

The strain rate quantifies the velocity at which the material is deformed and is directly linked to the type of manufacturing process and/or type of machine employed for that process as mentioned by [26,29]. For example, in processes such as sheet metal forming, extrusion and press forging, strain rates from 10^{-2} s^{-1} to 10^{2} s^{-1} are typically obtained, see [6]. These increase to rates ranging from 10^{2} s^{-1} to 10^{3} s^{-1} in high-speed manufacturing processes such as blanking or hammer forging, and higher still in machining operations, with strain rates between 10^{3} s^{-1} and 10^{6} s^{-1},see [3,16].

Previous studies, e.g. [29,43], have shown that in general increasing loading rates are translated into larger loads or energies during the forming processes, directly impacting in the overall cost of the manufacturing facilities. At the microstructural level, the loading rate, especially at high temperatures, has a direct effect on recrystallization kinematics and the resulting grain size of many metallic materials as shown by several authors as [8,23,42,48]. Consequently, it has a crucial

* Corresponding author at: Mondragon Unibertsitatea, Faculty of Engineering, Department of Mechanics and Industrial Production, Loramendi 4, Mondragon 20500, Gipuzkoa, Spain.
E-mail address: berice@mondragon.edu (B. Erice).

https://doi.org/10.1016/j.ijimpeng.2023.104764
Received 19 July 2022; Received in revised form 4 July 2023; Accepted 23 August 2023
Available online 28 August 2023

impact on the mechanical properties of the final component.

Although the macroscopical mechanical behaviour and the microstructural transformation phenomena of metals under intermediate-rate (10^2 s^{-1}–10^3 s^{-1}) metal forming conditions are of great industrial interest, fewer studies have been carried out in comparison to those performed at larger strain rates or at quasi-static loading regimes. One of the main reasons is that there are not many commercial experimental facilities that allow testing under intermediate-rate conditions as shown in [6]. Conventional servo-hydraulic testing machines are commonly utilised for quasi-static strain rate testing ($\leq$10 s^{-1}), and high strain rate tests (>10^3 s^{-1}) are generally performed in Split Hopkinson Pressure Bar (SHPB) testing machines, see [14] for more details. SHPB systems can be employed for intermediate strain rate testing between 10^2 s^{-1} and 10^3 s^{-1}, however, there are two main limitations: (i) the maximum strain achievable to deform the specimen at intermediate strain rates, and (ii) the validity of the force measurement due to wave overlapping.

Of course, several different solutions to avoid or circumvent the latter issue to certain extent have been proposed in the literature. For example, [12] propose to mitigate this by cleverly locating the strain gauges in the SHPB. Others, such as [31] use the deconvolution technique first proposed by [7], where through complex mathematical operations and three strain gauges attached to the output bar the force signal can be reconstructed even if wave overlapping exists, reducing the need of long output bars as in [39]. Using the same force measuring technique combined with a hydraulic jack that avoided the natural strain rate decrease exhibited by regular Hopkinson bar systems, [24] proved the effectiveness of such apparatus to get precise force measurements from quasi-static to dynamic regimes. With less mathematical finesse but equal effectiveness [32] are able to reconstruct the force signal without any deconvolution but with certain limitations [41] redesigned the output bar creating a series of concentric tubes welded to each other allowing the transmitted wave to travel further in these circumventing the overlapping issue.

Regarding the strain achievable with a given SHPB, the nature of the test defines the size of the system. For a given sample deformation, the lower the strain rate, the larger the SHPB system must be. Since in most metal forming processes the material is subjected to intermediate strain rates (<10^3 s^{-1}), and it is strained above 50%, a relatively large SHPB system would be needed. This, of course, has a significant impact on laboratory space and resources.

Numerous researchers have developed testing machines to perform mechanical characterisation tests at intermediate strain rates (e.g. tensile, compression or shear tests), as reviewed by [6]. Servo-hydraulic machines as those in [4,47], the hybrid testing apparatus in [20], drop towers employed by [25,33,38], flywheel devices used by [11,28,40] or modified SHPB systems such as in [12,31,34,41], amongst others, have been proposed as possible solutions to bridge the gap between quasi-static and high strain rate tests. However, as in the case of conventional SHPBs, excessive acquisition noise, limited achievable strain levels, and floor space are the main drawbacks of these machines. Furthermore, very few of these testing apparatuses are equipped with heating systems, which is a major limitation for characterising materials for high temperature processes and applications.

This paper presents a novel thermomechanical metal forming simulator developed to address this gap: the Automatic Thermo-Mechanical Tester (ATMT). This automatic laboratory testing machine is able to reproduce a wide range of real cold and hot industrial forming operations, from low strain rates (<1 s^{-1}) in an isothermal hydraulic press, up to intermediate strain rates (10^2 s^{-1}–10^3 s^{-1}) in a Direct Impact Drop Hammer (DIDH) apparatus. Additional forming strategies can also be tested, including intermediate heating cycles and combined strain rate deformations. Moreover, by modifying the sample geometry and the tooling of the forming modules, several loading conditions, such as compression, tension or shear, can also be analysed in the ATMT.

The DIDH apparatus, the high-speed forming module of the ATMT, was developed as an intermediate strain rate (10^2 s^{-1}–10^3 s^{-1}) mechanical testing device for metal forming operations. This high-speed testing machine presents numerous challenges, such as high-rate data acquisition, accurate load measurement or specimen visualisation throughout the test. It is the focus of the current investigation to validate such an apparatus as a reliable testing machine for intermediate strain rates. To this end, the cylindrical uniaxial compression tests of three materials, the S235JR structural steel, OFHC copper and the Inconel 625 nickel-based superalloy, were performed at various intermediate strain rates and high temperatures in the DIDH. Additional SHPB tests on one of the afore-mentioned materials were conducted for the sake of comparison. Finally, a detailed Finite Element (FE) numerical study of the system that included the calibration of a visco-plastic J2 plasticity model for the S235JR steel and its verification was carried out. The aim of the numerical study was on the one hand, to assess the effect that the specimen geometry had on the strain rate evolution throughout the DIDH tests, and on the other hand, to identify and to analyse the source of the experimental force signal's oscillations for further future improvements.

2. The DIDH as an intermediate rate testing apparatus

The Automatic Thermo-Mechanical Tester (ATMT) can reproduce a wide range of real hot and cold industrial metal forming conditions, from low strain rates (<1 s^{-1}) present for example in extrusion processes, up to elevated strain rates (>100 s^{-1}) in hammer forging processes. The testing device is composed of four main modules: a sample heating furnace, an array of quenching tanks, an isothermal hydraulic press for low strain rate testing (<1 s^{-1}), and the Direct Impact Drop Hammer (DIDH) for intermediate strain rate testing (>100 s^{-1}) (see Fig. 1). The DIDH was developed to overcome the difficulties encountered in performing intermediate strain rate tests (10^2 s^{-1}–10^3 s^{-1}) with universal hydraulic testing devices and SHPB systems. The furnaces installed in the ATMT for the sample conditioning and the isothermal press use electric resistors giving a maximum temperature of 1350 °C. To minimise human error the system is fully automated, and the sample manipulation is carried out by an electro-pneumatic system integrated into the machine.

A wide variety of industrial forming processes that require multi-stage loading or heating conditions, that can individually or jointly include non-proportional loadings, different heating cycles or varying loading rates, can be simulated by controlling the test parameters or adapting the tooling of the forming modules.

In the current study we focus on the pneumatically actuated DIDH. This mechanical module is mounted vertically and is comprised of a 92 kg hammer that is pushed downwards by a high-pressure pneumatic cylinder propelling it towards the anvil, the fixed part of the system (see Fig. 2). The specimen is located between the hammer and the anvil as shown in Fig. 2. For the moment, and for safety reasons, the hammer is equipped with a metallic cover that fully encloses the specimen during the testing procedure. This cover and the anvil are marked with white dots that are easily trackable with a number of current commercial Digital Image Correlation (DIC) software. The hammer height is adjustable in height which allows the impact velocities to range from 2.5 up to 5 m/s. With these specifications the DIDH gives a maximum applicable deformation energy of 1.15 kJ. The anvil is instrumented with a piezoelectric force sensor (Kistler 9106A) allowing for direct force measurements.

The hammer velocity v_{hmr} can be calculated from a simplified free body diagram of the hammer as illustrated in Fig. 3(a). The equation of motion then reads,

$$m\frac{dv_{hmr}}{dt} = pA + mg - \underbrace{f_R}_{\ll 1} \tag{1}$$

where $m = 92$kg is the combined mass of the hammer and pneumatic cylinder, $p = 6.5$bar is the pressure given by the constant pressure

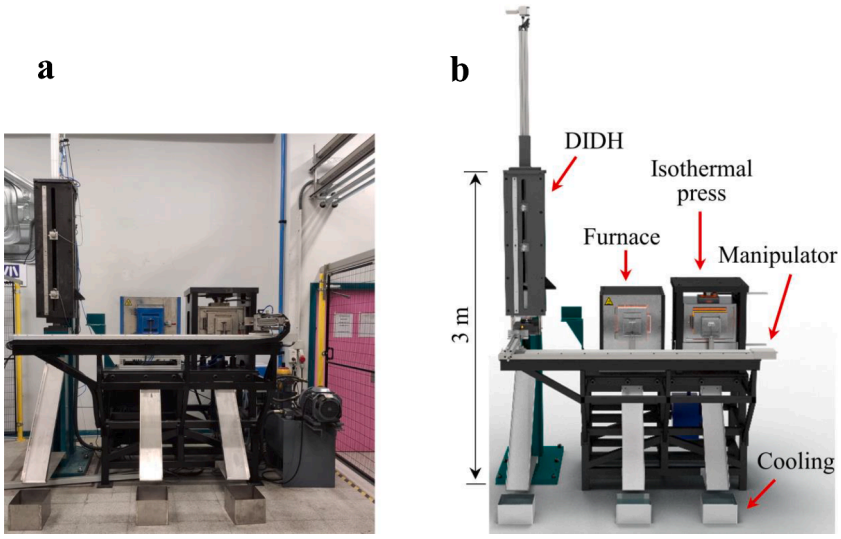

Fig. 1. Overview of the Automatic Thermo-Mechanical Tester (ATMT) (a) Real laboratory picture and (b) 3D render from CAD.

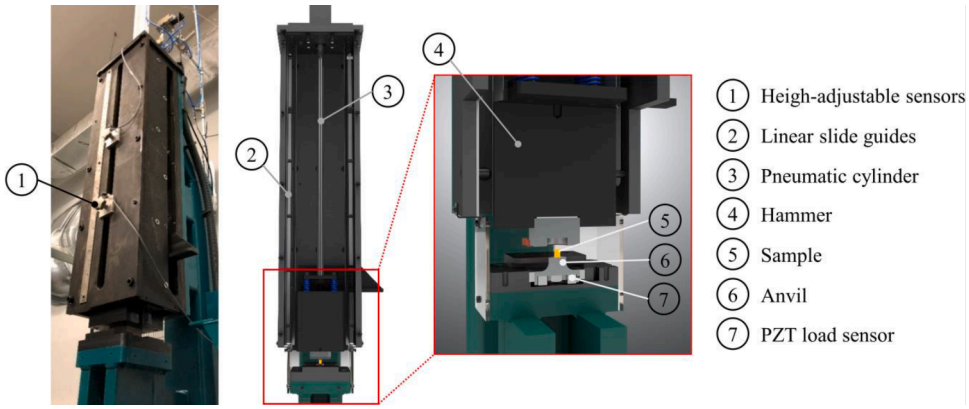

Fig. 2. Compression test setup in the DIDH.

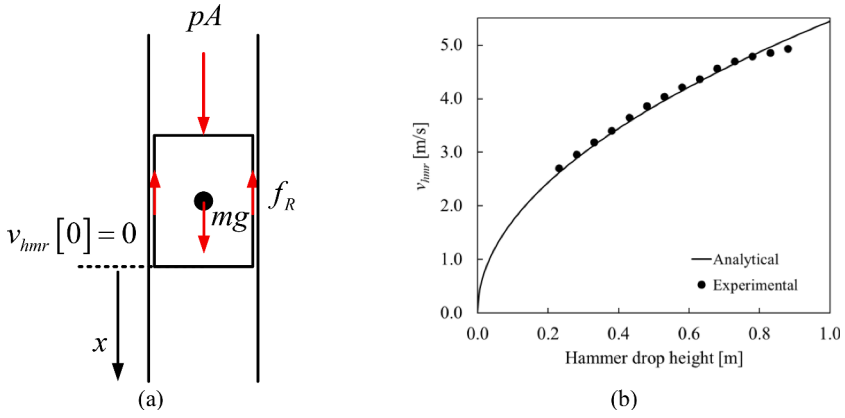

Fig. 3. (a) Simplified free body diagram of the drop hammer. (b) Hammer velocities vs. the drop height measured with the high-speed camera (black dots) compared against the analytical approach (black curve).

regulator behind the cylinder, A is the cross-section area of the cylinder with a diameter 30 mm and f_R is the friction between the cylinder and the hammer with the guiding system that will be considered negligible. The hammer is stationary at $x = 0$, i.e. $v_{hmr}[0] = 0$. Using the chain rule and arranging Eq. (1) we get,

$$v_{hmr} dv_{hmr} = \left(p\frac{A}{m} + g\right) dx \tag{2}$$

Integrating yields the hammer velocity as a function of the drop height as:

$$v_{hmr}[x] = \sqrt{2x\left(p\frac{A}{m} + g\right)} \tag{3}$$

The result of this simplified analytical calculation was compared against the hammer velocities calibrated for different drop heights obtained post-processing the images acquired with a high speed camera (for more details see Section 4) in Fig. 3 showing an excellent agreement. This simple equation was able to accurately calculate hammer impact velocities, at least within the 2.5 to 5 m/s range.

3. Materials description

The cylindrical specimens (see Table 1) used to conduct the experiments in this investigation were machined from three different easy to source metallic materials that represented iron-based, copper-based and nickel-based alloys:

- Heavily used in structural applications, the S235JR grade is a low carbon content ferritic-perlitic structural steel which is widely used for welding, fastening, and as part of structural components, especially in civil engineering. Its chemical composition is reported in Table 2. All specimens were machined from a 20 mm thick hot rolled steel sheet.
- The high-purity Oxygen-Free High-Conductivity (OFHC) copper (>99.99% Cu), apart from its obvious applications, has been broadly used as a benchmark in high loading rate mechanical testing due to its low strain rate sensitivity. The samples were cut from a 15 mm diameter bar.
- The Inconel 625 is a solid-solution strengthened nickel-base superalloy. The high nickel content combined with a considerable proportion of specific alloying elements, such as chromium or molybdenum (see certified chemical composition in Table 3), provides excellent mechanical and corrosion properties in aggressive environments, from cryogenic to high service temperatures. For this reason, it is widely used in aeronautical, petrochemical, energy generation, and marine applications. A 160 mm diameter bar (ASTM B446–19 standard) was machined to obtain the specimens.

4. Direct impact drop hammer experiments

4.1. Experimental setup

Cylindrical compression specimens with nominal diameter D and length L, reported in Table 1, were tested at different impact velocities and temperatures. The steel and copper specimens were tested at room temperature with varying hammer velocities of 3.3, 4.0, 4.7 and 5.0 m/s, while the Inconel 625 experiments were conducted at 4.0 m/s at 950, 1050 and 1150 °C. Three repetitions were performed for each condition in which a very low deviation was observed.

To monitor the hammer movement, a Photron Fastcam-APX RS250K high-speed camera with appropriate illumination lamps was utilised (see Fig. 4). It was set up to record at 15000fps with a resolution of 256 × 512px^2. A coarse random grid of the white dots on a dark background was generated and applied to the hammer (moving) and anvil (static) surfaces for subsequent DIC analysis (see Fig. 2). Due to its relatively large mass and volume with respect to the specimen, the hammer was considered as rigid body for the DIC analysis and the specimen length history $l[t]$ was obtained from the displacement history of the hammer, which was calculated by post-processing the high speed camera images with the GOM Correlate DIC [13].

To obtain the force histories $F[t]$, a Kistler 9106A piezoelectric force sensor mounted directly in the anvil was employed in combination with a Tektronix TSD 2004B oscilloscope with an acquisition frequency of 300 kHz. The axial engineering strain and stress histories were computed using the following expressions:

$$e[t] = \frac{l[t]}{L} - 1 \tag{4}$$

$$s[t] = \frac{F[t]}{A} \tag{5}$$

where $A = \pi D^2/4$ is the initial cross-section area of the specimen. The strain rate was calculated as:

$$\dot{e}[t] = \frac{1}{L}\frac{\Delta l}{\Delta t} \tag{6}$$

with $\Delta l = l[t+\Delta t] - l[t]$ and assuming $\dot{e}[0] = 0s^{-1}$.

In the high temperature tests, the sample was first heated in the furnace, then automatically carried from the furnace to the DIDH, a process that took 5 s, and finally compressed by the hammer. To be able to reach the target forging temperatures, the cooling suffered by the specimen during the 5 s manipulation window had to be compensated increasing the initial furnace temperature. This was corrected monitoring the temperature in a control specimen that had a K-type thermocouple placed inside it (a 0.75 mm diameter hole was drilled to the centre of a sample) throughout the entire testing procedure for several initial furnace temperatures. A five minute pre-test heating time was found to be sufficient to reach and homogenise the sample temperature, and thus, this heating time was utilised in the experimental campaign. All samples were water quenched in less than 2 s potentially allowing subsequent microstructural analysis. Such a study is out of the scope of this paper, and therefore, it is not included here. Although this is an ongoing investigation currently being investigated by the authors, for more details on this subject, the readers are referred to [2].

Table 2
Chemical composition in wt.% of S235JR structural steel (EN 10,025–2:2004 standard).

C max.	Mn max.	Si max.	P max.	S max.	N max.	Cu max.	CEV max.
0.17	1.40	–	0.040	0.040	0.012	0.55	0.35

Table 3
Chemical composition in wt.% of Inconel 625 nickel-based superalloy.

Ni min.	Cr	Mo	Fe max.	Nb+Ta	Co max.
58.0	20.0–23.0	8.0–10.0	5.0	3.15–4.15	1.0

Mn max.	Si max.	Mn max.	Ti max.	C max.	P max.	S max.
0.5	0.5	0.5	0.4	0.1	0.015	0.015

Table 1
Cylindrical specimen geometries for the three materials.

	S235JR steel			OFHC copper		Inconel 625	
	Quasi-static	DIDH	SHPB	Quasi-static	DIDH	Quasi-static	DIDH
D [mm]	13.50	13.50	6.87	15.00	15.00	10.00	10.00
L [mm]	20.00	20.00	9.90	19.80	22.50	15.00	16.00

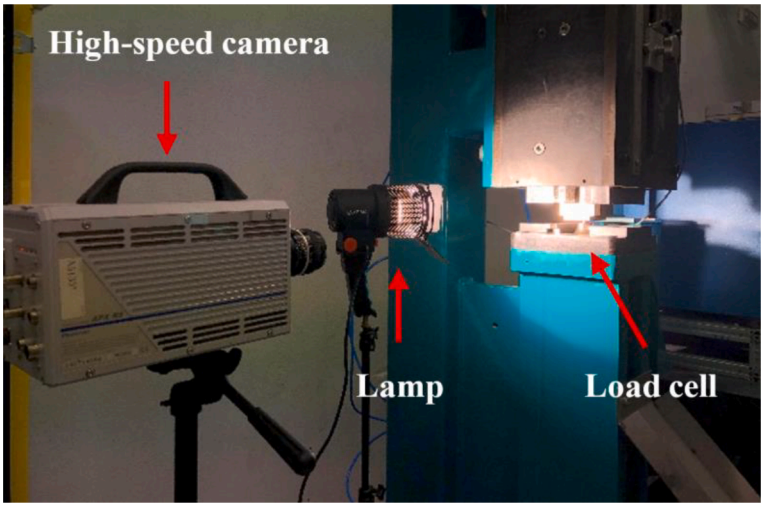

Fig. 4. Data acquisition set-up in the DIDH.

4.2. Results and discussion

The results of a representative test at a hammer velocity of 4 m/s for the three different materials tested in the DIDH are presented in Fig. 5. The axial engineering strain histories calculated with Eq. (4) are represented with red dots, and the black dots denote the stress histories calculated with Eq. (5). Fig. 5 also shows the difference in acquisition rate of the load sensor and the high-speed camera. The displacement histories were linearly interpolated on the load cell time base to construct the axial engineering stress-strain curves depicted in Fig. 6 (a–c). The strain rate-strain curves plotted in Fig. 6(d–f) only needed the data extracted from the DIC analysis of the high-speed camera images.

Only the hammer displacement histories were used to calculate the strains, neglecting the elastic deformation and movement of the anvil. The latter was monitored for all cases. In the most unfavourable case, the maximum displacements of the anvil and hammer were 0.32 mm and 11.67 mm respectively, being the displacement of the anvil only a 2.74% of that of the hammer. As a reference, quasi-static compression tests are depicted in light colour in Fig. 6(a–c). These were carried out in a Instron-4206 servo-hydraulic universal testing machine equipped with a

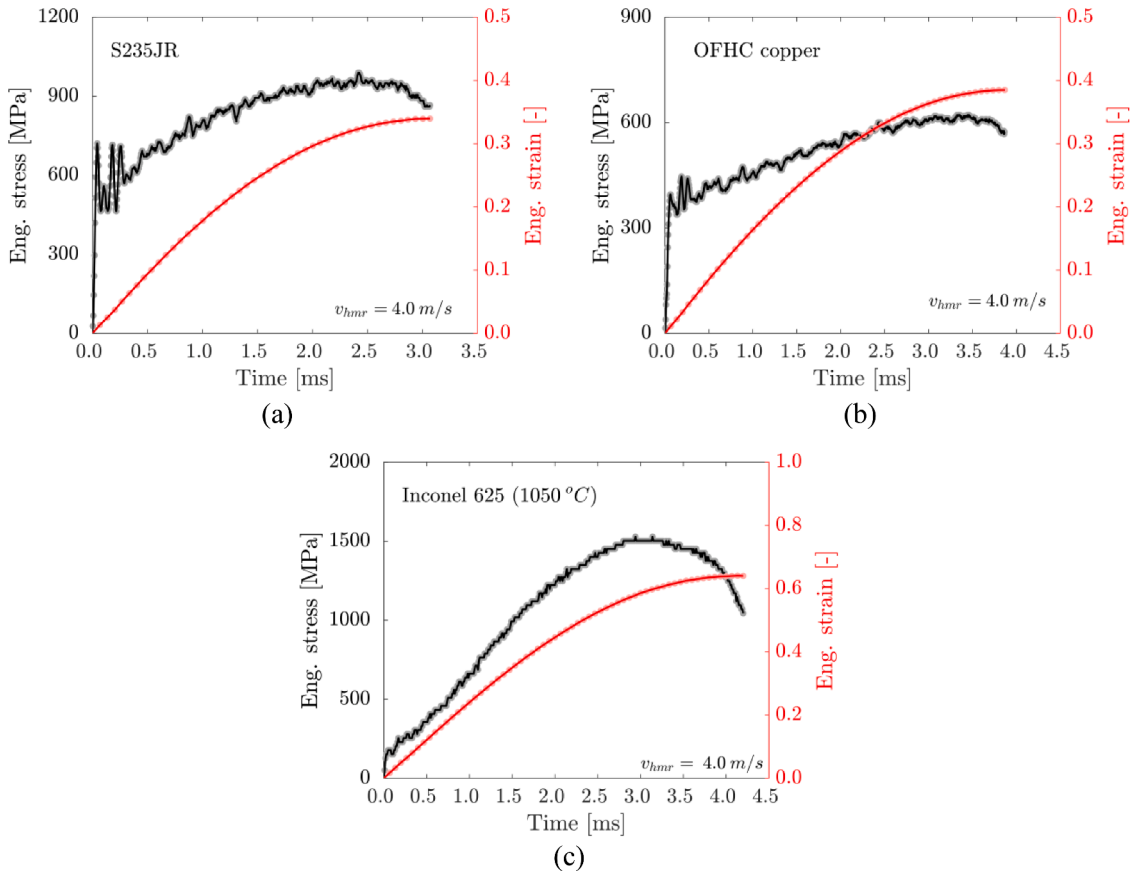

Fig. 5. Engineering strain and stress histories for DIDH tests conducted at a hammer velocity of 4.0 m/s for the (a) S235JR steel, the (b) OFHC copper and the (c) Inconel 625 (1050 °C).

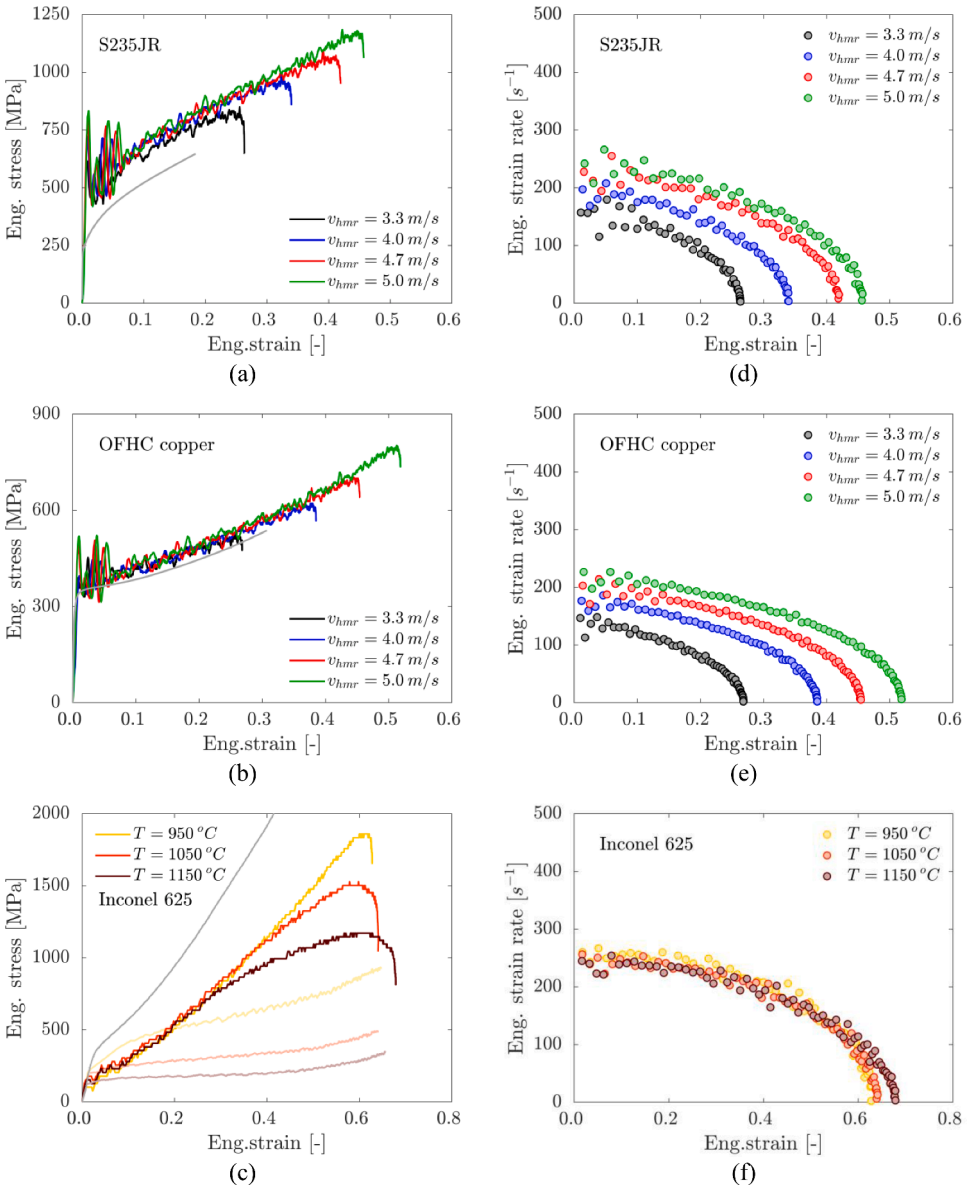

Fig. 6. (a-c) Axial engineering stress-strain curves and (d-f) strain rate-strain curves obtained from the DIDH room temperature tests with hammer velocities of 3.3m /s (black), 4m /s (blue), 4.7m /s (red), and 5m /s(green) for the S235JR steel and the OFHC copper; and at 4m /s and temperatures of 950 °C, 1050 °C and 1150 °C for the Inconel 625 nickel-based superalloy. Quasi-static compression tests are depicted in light colour (grey at room temperature and coloured at high temperatures).

100 kN load cell and compression platens at nominal strain rates of 10^{-3} s^{-1} (0.1 s^{-1} for the Inconel 625 at high temperatures) averaged over the specimen gauge lengths (see Table 1 for specimen geometries).

In general, Fig. 6a and b show that higher hammer velocities led to larger sample deformations and flow stresses. The effect of the loading rate on the mechanical behaviour of the S235JR steel, although mild for the loading rates tested, is noticeable. However, the rate dependency in the OFHC copper is barely appreciable. It is only through comparison with the quasi-static response that one can observe the effect of the strain rate. These trends were in accordance with the well-established strain rate sensitivity effects for similar materials as shown by other authors as [17,30,18,10,44].

The large change in impedance between hammer and specimen as well as the stress wave propagation in the system, lead to some oscillations in the force readings particularly at the beginning of the DIDH curves, as it can be observed in both Figs. 5 and 6. However, these fade out to certain extent as tests progress leaving the piezoelectric load cell noise as the only source of the oscillations. At a first glance, these initial oscillations might be attributed to inertia effects and consequentially to the lack of the dynamic equilibrium of the specimen. Let us assume that we have a metallic cylindrical specimen in which elastic waves are propagated one-dimensionally such that $c = \sqrt{E/\rho} \simeq 5000\text{m/s}$. The characteristic time for such specimen, calculated as $t_c = 2L/c$, would be for the worst case scenario, i.e. $L = 22.5\text{mm}$, $t_c = 9\mu\text{s}$. From the stress or force histories we know that the first oscillation's peak in all cases is close to $50\mu\text{s}$. This means that for the worst case scenario the waves have travelled more than 5 roundtrips inside the specimen, which is generally considered as a threshold for the specimen to be under dynamic equilibrium. It is therefore unlikely to attribute these oscillations to the lack of dynamic equilibrium. This will be discussed in length later in the article with the support of the FE simulation results.

Fig. 6(d–f) also show that far from being constant, the engineering strain rate decreased as the specimen was compressed. As soon as the hammer came into contact with the sample, it started to decelerate until its kinetic energy was almost depleted, point at which the specimen

could not deform anymore. However, this strongly depends on the specimen geometry and the work hardening of the material as these factors dictate the amount of energy needed to deform them. Fig. 6(d and e) show very similar responses, as the specimens tested for the S235 steel and the OFHC copper were very similar in size and both materials exhibited very pronounced work hardenings. The OFHC copper however, seemed to maintain a more constant strain rate, at least for the higher hammer velocities. If we take a maximum engineering strain of 0.3 for the OFHC copper, the maximum at which the quasi-static tests were performed, the variation in strain rate for hammer velocities of 4.7 and 5.0 m/s are 65 (32.5% of the maximum strain rate) and 60 s^{-1} (25% of the maximum strain rate) respectively. Surely, if for the same straining a more constant strain rate is sought, the energy available to deform the specimen should be increased. This could be done by maintaining the same specimen geometry and increasing the kinetic energy of the hammer or by keeping the configuration of the hammer as it is and modifying the specimen geometry as will be shown later in Section 6.2. In any case, the non-constant strain rate does not pose any issue if computational models are to be calibrated by inverse FE simulations employing adequate boundary conditions. This is also analysed with more detail in Section 6.2.

The high temperature tests at intermediate strain rate (Fig. 6(c) dark coloured curves), from 1050 to 1350 °C, conducted on the Inconel 625 exhibited anomalous, or at least counterintuitive, behaviour compared to that observed under quasi-static conditions (Fig. 6(c) light coloured curves). The strength of the latter decreased with increasing temperature, while the strength of the formers were virtually identical for all three temperatures, at least until the specimens were largely deformed, well over 25% of engineering strain. This has its origin in the microstructural changes that the material undergoes during the heating and deformation process, more specifically, the dynamic and post-dynamic recrystallization are the phenomena responsible for such stress-strain response. The extensive microstructural study carried out by the authors confirmed that these microstructural changes were indeed responsible for the stress-strain behaviour that was observed. As it has been previously mentioned, such a study has been considered to be out of the scope of the current article and as such it is not included here.

5. Split Hopkinson pressure bar experiments

SHPB tests were conducted for experimental comparison and computational model calibration purposes. Therefore, only one of the three analysed materials was tested in such device, i.e. the S235JR.

The configuration of the SHPB employed to perform the compression tests is schematically depicted in Fig. 7. The striker, input and output bars are made out of steel with a mass density of $\rho_b = 7850\text{kg}/\text{m}^3$, and a calibrated elastic wave propagation speed of $c_b = 5100\text{m}/\text{s}$. The SHPB system and test methodology is well established in the literature, see [14] for details. The strain histories measured at the strain gauge locations, shown in black in Fig. 7, were shifted to the specimen-bar interfaces and decomposed into incident, reflected transmitted signals as in [22]. These, denoted as $\varepsilon_{I,R,T}[t]$, were used to calculate the force and the velocity in the interfaces of the input and output bars. However, here only the output force measurement, $F[t] = \varepsilon_T[t]E_bA_b$, was employed to get the force histories. To measure the specimen length history $l[t]$, a Phantom v2511 high-speed camera was set to record 150.000fps, with an exposure of 0.92μs at resolution of $384 \times 288\text{px}^2$, taking one picture every 6.6μs. A telecentric lamp equipped with a led source that illuminated the specimen from the back was used to obtain a high degree of grey value contrast, allowing easy tracking of the bar and specimen edges. The specimen length history $l[t]$ was computed employing the point tracking technology available in eCorr v4 DIC software Fig. 8). The engineering strain and strain rate histories were calculated as in Eqs. (4) and ((6), respectively. In the present study, the striker was launched at three velocities 5.8, 8.3 and 10.7 m/s to obtain different loading rates. These velocities were measured with a laser right before the striker impacted the input bar.

As in the DIDH tests the acquisition frequency was shorter for the force measurements. However, the camera used in these tests had such a short acquisition frequency that the differences were between the stress and strain history frequencies were minor. The axial engineering stress-strain and strain rate-strain curves of all the tests conducted in the SHPB are depicted in Fig. 9(a) and (b), respectively. Although the results were significantly "cleaner", showing way less oscillations in the stress-strain curves, the limitations of the SHPB system in performing intermediate strain rate tests can be clearly seen in this plot. For an average engineering strain rates of $\dot{e}_{avg} = 400\text{s}^{-1}$, $\dot{e}_{avg} = 150\text{s}^{-1}$ and $\dot{e}_{avg} = 90\text{s}^{-1}$ the maximum engineering strains were only $e_{\max} = 0.3$, $e_{\max} = 0.1$ and $e_{\max} = 0.075$. For similar strain average strain rates, the maximum strain levels achieved in the DIDH were significantly larger. This is directly linked to the SHPB system limitations mentioned in the introduction. Although the configuration of the output bar allows for a maximum pulse length of $t_F = 2(L_{out} - L_{SGi})/c_b \simeq 1170\mu$sbefore the waves overlap, the length of the striker limits the test duration to $T = 2L_{str}/c_b \simeq 650\mu$s. Therefore, the specifications of the gas gun used to launch the striker and the laboratory space were the bottleneck for this system. It should be noted that we are only highlighting the limitations of the current SHPB system when it comes to the intermediate strain rate testing.

The effect of the loading rate in the flow stress is clearly visible in Fig. 9(a), exhibiting a significant increase for larger loading rates. Although not constant, the strain rate seemed to plateau as the specimen got compressed. If the specimen could have been strained to larger compression levels the strain rates would have tended towards these plateau values.

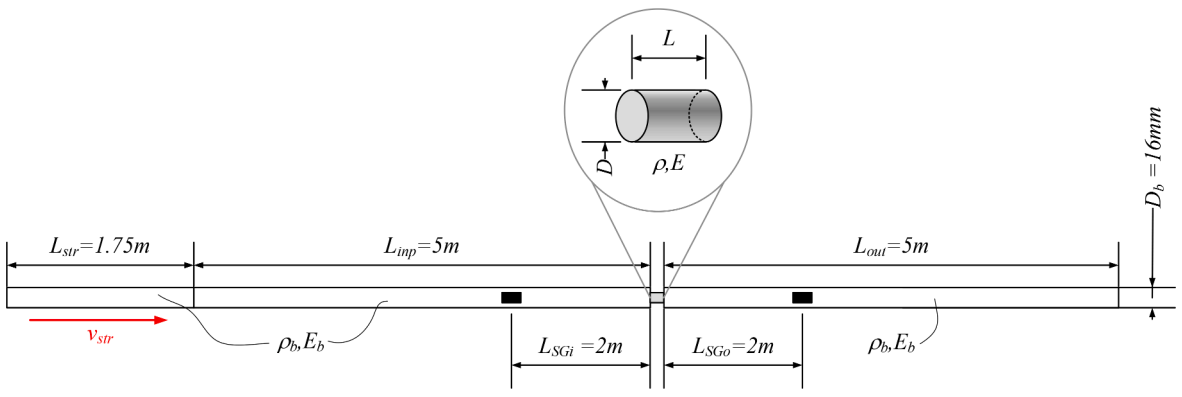

Fig. 7. SHPB system comprised of a striker, an input and an output bar of equal lengths.

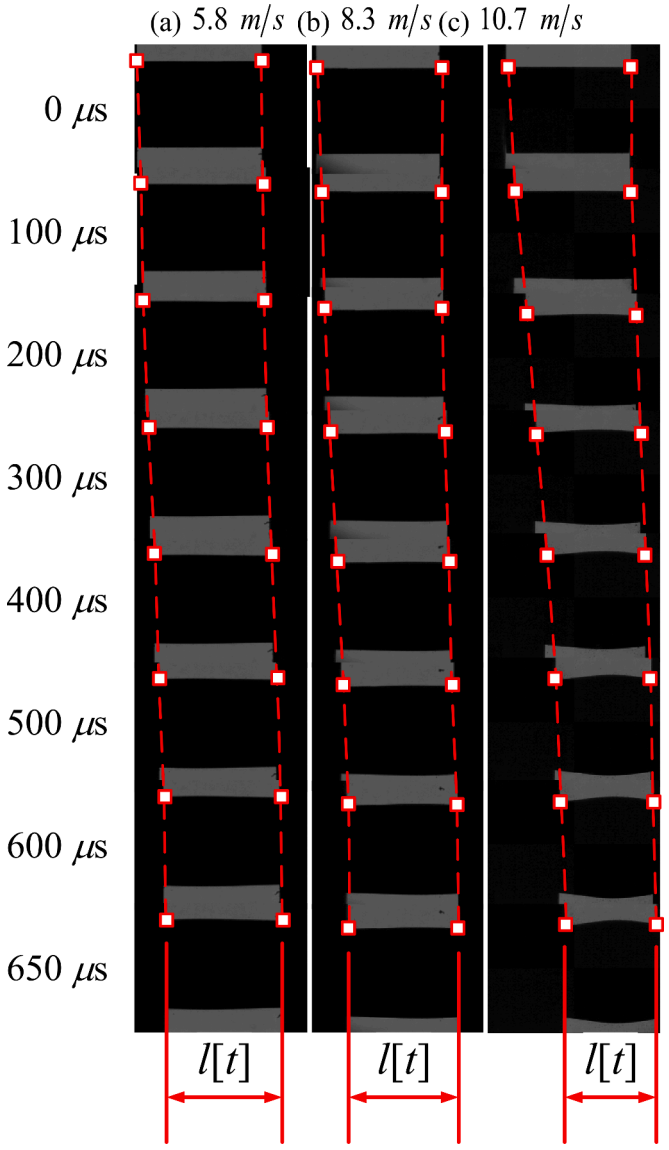

Fig. 8. Image sequence of the deformed specimens from which the instantaneous length was computed. The squares indicate the points tracked throughout the tests.

6. Numerical study

A numerical study, where a simplified and a full-scale model were simulated, was performed to assess several relevant elements observed in the experiments and other significant aspects such as the feasibility of using the DIDH tests for material calibration or the effect of the specimen geometry on the strain rate. A simple classical associated J2 plasticity combined with a Johnson-Cook-type work hardening was calibrated for the S235JR steel to conduct such an analysis. Details of the model as well as of the calibration procedure are given subsequently.

6.1. Computational model

The constitutive equations have been formulated in a rotationally neutralised configuration where we transform the Cauchy stress $\mathbf{\Sigma}$ and rate-of-deformation $\mathbf{D}$ tensors as follows,

$$\boldsymbol{\sigma} = \mathbf{R}^T \cdot \mathbf{\Sigma} \cdot \mathbf{R} \; and \; \mathbf{d} = \mathbf{R}^T \cdot \mathbf{D} \cdot \mathbf{R} \tag{7}$$

where $\mathbf{R}$ is the rotation tensor from the polar decomposition of the deformation gradient $\mathbf{F} = \mathbf{R}\cdot\mathbf{U} = \mathbf{V}\cdot\mathbf{R}$. Assuming the additive decomposition of the corotational rate-of-deformation tensor, the rate form of the linear elastic isotropic law is defined by:

$$\dot{\sigma} = \mathbb{C} : \mathbf{d}^e = \mathbb{C} : (\mathbf{d} - \mathbf{d}^p) \tag{8}$$

where $\mathbb{C}$ is the isotropic elastic stiffness fourth-order tensor that contains the elastic moduli.

The well-known von Mises yield function, given by:

$$f[\boldsymbol{\sigma}, \sigma_Y] = \overline{\sigma}[\boldsymbol{\sigma}] - \sigma_Y \tag{9}$$

is chosen to describe the plastic yielding. As usual, $\overline{\sigma} = \sqrt{\frac{3}{2}\mathbf{s} : \mathbf{s}}$ is the von Mises stress and $\mathbf{s} = \mathrm{dev}[\boldsymbol{\sigma}]$. The work hardening σ_Y is a Johnson-Cook-type law ([18]) following the expression:

$$\sigma_Y = \left\{\sigma_0 + \sum_{i=1}^{2} Q_i(1 - \exp[-C_i p])\right\}\left\{1 + C\ln\left[\frac{\dot{p}}{\dot{p}_0}\right]\right\}\left\{1 - \left(\frac{T - T_r}{T_m - T_r}\right)^m\right\} \tag{10}$$

where $p = \int_0^t \dot{p} dt$, is the equivalent plastic strain, $\dot{p} = \sqrt{\frac{2}{3}\mathbf{d}^p : \mathbf{d}^p}$ is the equivalent plastic strain rate, T is the temperature, σ_0 is the yield stress, Q_1, C_1, Q_2, C_2 are the constants of the two-term Voce strain hardening law, C is the strain rate coefficient, $\dot{p}_0$ is the reference strain rate, m is the thermal softening exponent, T_r is the reference temperature and T_m is the melting temperature.

The flow rule is chosen to be associative,

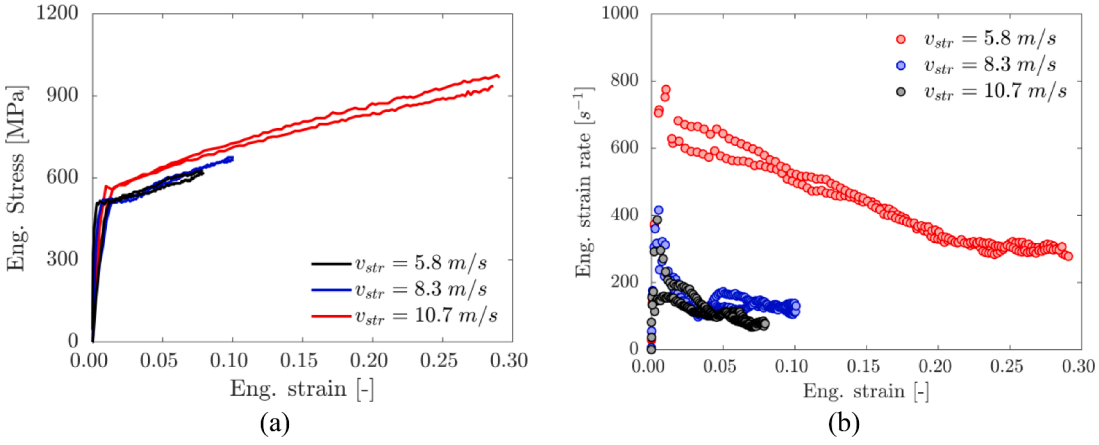

Fig. 9. (a) Axial engineering stress-strain curves and (b) strain rate-strain curves obtained from the SHPB tests with striker velocities of 5.8m /s (black), 8.3m /s (blue) and 10.7m /s (red).

$$\mathbf{d}^p = \frac{\partial f}{\partial \boldsymbol{\sigma}} = \dot{\lambda}\frac{3}{2}\frac{\mathbf{s}}{\bar{\sigma}} \tag{11}$$

From the work conjugacy, $\boldsymbol{\sigma} : \mathbf{d}^p = \bar{\sigma}\dot{p}$, the evolution equation for the plastic strain is $\dot{p} = \dot{\lambda}$ and considering adiabatic heating conditions, the temperature evolution is $\dot{T} = \frac{\chi}{\rho C_p}\boldsymbol{\sigma} : \mathbf{d}^p$, where ρ is the mass density, C_p is the specific heat and χ is the Taylor-Quiney coefficient. The constitutive model equations were implemented in their incremental form as a user material subroutine in ABAQUS/Explicit, [1], non-linear explicit time integration FE solver.

The material constants were identified through inverse modelling with an iterative domain reduction scheme available in LS-OPT (see [21]) where the error is minimised between experimental and numerical stress-strain responses. The number of constants and their diverse effects on the material's response led to a complex interplay amongst them, which possibly could give more than one constant set fitting such experimental data, somehow dispossessing constants from their corresponding physical meaning. To avoid this, a pragmatic sequential identification procedure was employed, where (i) quasi-static uniaxial tensile tests were used to calibrate the strain hardening, (ii) quasi-static uniaxial compression tests were used to obtain the friction coefficient, and (iii) dynamic compression performed in the SHPB with striker velocities of $8.3m/s$ and $10.7m/s$ were utilised to calibrate the strain hardening and thermal softening of the Johnson-Cook model.

The experiment carried out with the lowest striker velocity, i.e. $5.8m/s$, did not show a substantial change over the next higher velocity. Further, as discussed in the previous section, the compressive pulse was not long enough to generate a sufficiently long test duration that would have allowed obtaining a more representative stress-strain curve. Hence, it was not used for the calibration. Additional quasi-static uniaxial tensile and compression tests were conducted to calibrate the work hardening of the computational material model used in the finite element simulations and to estimate the friction coefficient between the platens and the specimen in the case of the compression tests. The quasi-static tensile tests were performed on ASTM E8M standard dogbone specimens in a Instron-4206 servo-hydraulic universal testing machine equipped with a 100 kN load cell at a strain rate of 10^{-3} s^{-1} averaged over a gauge length of 60 mm.

Making use of the specimens' symmetry, only one-eighth (tensile specimen) and one-fourth (compression specimen) of the finite element models were discretised with $0.5 \times 0.5 \times 0.5$ mm^3 C3D8R eight-node reduced-integration elements with hourglass control available in ABAQUS/Explicit ([1]). The experimentally measured velocities were applied as prescribed boundary conditions. The quasi-static cases were run with mass-scaled solutions that gave approximately 10^5 time increments throughout the complete simulation time. To simulate the barrelling observed in all the compression experiments, as shown in Fig. 11, the compression tests were simulated with a friction coefficient $\mu = 0.3$ between platens (rigid surfaces) and specimen that was estimated by measuring and comparing the final geometry of the quasi-static specimen (see Fig. 11(a)).

The resulting engineering stress-strain curves are compared against the experiments in Fig. 10 showing an excellent agreement. The material constants resulting from the optimisation procedure are reported in Table 4. The axial cross-section of the compression specimens with equivalent plastic strain contours two striker velocities used in the calibration procedure 8.3 and 10 m/s are shown in Fig. 12(a) and (b) respectively, also allowing the direct comparison of the deformed profiles with the experiments. For illustration purposes, the calibrated material's equivalent stress-plastic strain curves for several constant plastic strain rates are plotted in Fig. 15.

6.2. Simplified DIDH simulations

The simplified FE simulations of the DIDH experiments used the same element size and configuration, including the friction coefficient, as those used in the quasi-static compression tests. No mass scaling was employed in this case. The hammer weight was modelled with a nodal mass of 92 kg attached to the top rigid surface that had an imposed initial velocity. The gravity effects were neglected since they were small compared to the energy generated by the DIDH. Alternatively, one could use the displacement histories measured in the experiments as prescribed motions on the rigid surfaces. However, this would imply a precise monitoring of the hammer motion by DIC or similar methods, as is the case here. With this simple numerical setup, the hammer velocity calculated from the equation of motion (Eq. (3)) could be directly used as a boundary condition. The resulting engineering stress-strain (black) and strain rate-strain (red) responses are plotted in continuous lines in Fig. 13 for hammer velocities of 3.3m/s (a), 4m/s (b), 4.7m/s (c), and 5m/s(d). The calibrated model's mechanical response was in excellent agreement with the experimental data. But more importantly, the results showed that this numerical setup could adequately describe the DIDH tests.

6.2.1. Effect of the specimen size in the DIDH tests

As previously mentioned, the average engineering strain rate for the specimen geometry tested decreased over time as the kinetic energy of the hammer was employed to deform the sample almost until it was depleted, i.e. until the hammer rebounded. Simulations with a hammer velocity of 4.7 m/s were repeated with different specimen sizes to assess

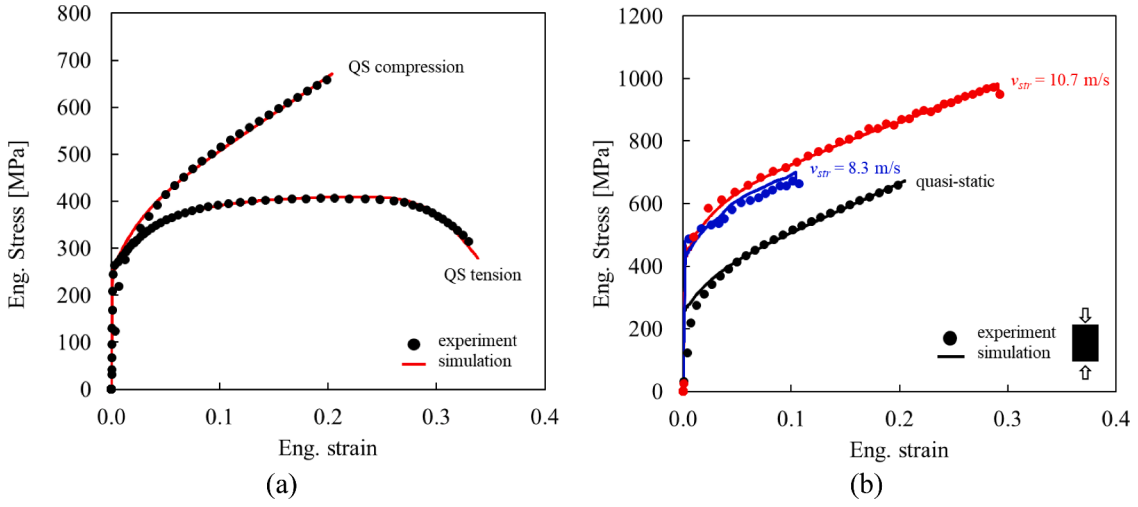

Fig. 10. Axial engineering stress strain curves of the quasi-static (a) and dynamic (b) tests employed in the S235JR material constant identification procedure.

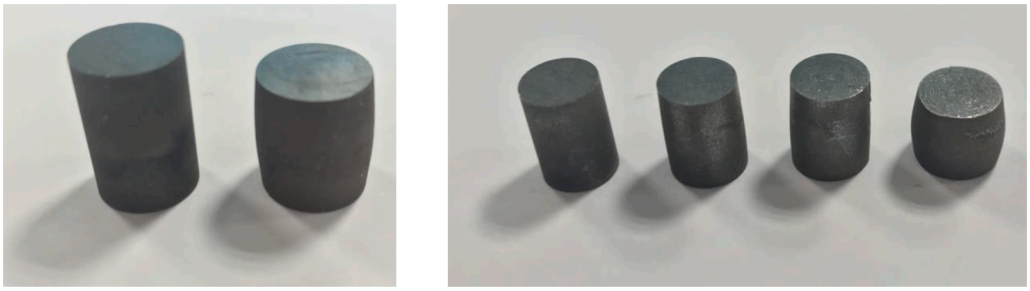

(a) (b)

Fig. 11. Quasi-static (a) and dynamic (b) post-test compression sample geometries.

Table 4
Johnson-Cook material constants for the S235JR low-alloy steel.

Elastic constants and physical properties				
E[GPa]	ν	ρ[kg /m^3]	$C_p\left[\frac{J}{kg^oC}\right]$	T_m[^{o}C]
200	0.33	7850	460	1500
Voce strain hardening				
σ_0[MPa]	Q_1[MPa]	C_1	Q_2[MPa]	C_2
250.00	105.00	35.24	330.00	3.00
Johnson-Cook strain rate hardening and thermal softening				
C	$\dot{p}_0$[s^{-1}]	m	χ	T_r[^{o}C]
0.0545	1.0×10^{-3}	0.375	0.9	25

the effect that this had on the strain rate. Maintaining the length to diameter aspect ratio constant, $L/D = 1.5$, the specimen diameter D was reduced to $3D/4$ and $D/2$. In the same fashion as that shown in Fig. 13, the engineering stress-strain and strain rate-strain responses are plotted in Fig. 14. We can observe how the strain rate always decreases with increasing strain. However, for similar deformation energies per unit volume, i.e. approximately the areas under the stress-strain curves, the situation changes drastically. If we compare the responses until a maximum strain of 0.4, the strain rate for the largest specimen varies from 250 to 60 s^{-1}, for the intermediate size goes from 310 to 240 s^{-1} and for the smallest it hardly changes from 470 to 460 s^{-1}.

6.2.2. *Alternative calibration with the DIDH experiments*

To assess the potential that the DIDH experiments might had as calibration data, the material constants controlling the loading-rate effects, i.e. C and m were recalibrated following the same procedure as that explained in Section 6.1, but this time the stress-strain curves from DIDH tests were used for the minimisation problem. The constants obtained, $C = 0.0445$ and $m = 0.445$ (cal. HMR), differed sightly from those in Table 4 (cal. SHPB). However, the overall adiabatic behaviour does not change significantly as shown in Fig. 15 for a constant equivalent strain rate of 500 s^{-1}. The SHPB and DIDH were simulated with the new set of constants to evaluate the validity of the latter as potential calibration data.

Fig. 16 shows the engineering stress-strain curves obtained from the numerical simulations of the SHPB tests in (a-b); and the numerical stress-strain responses of the DIDH tests in (c-f). The numerical simulations performed with the cal. SHPB (red dashed curves) gave larger stresses than those carried out with the cal. HMR (black curves) for

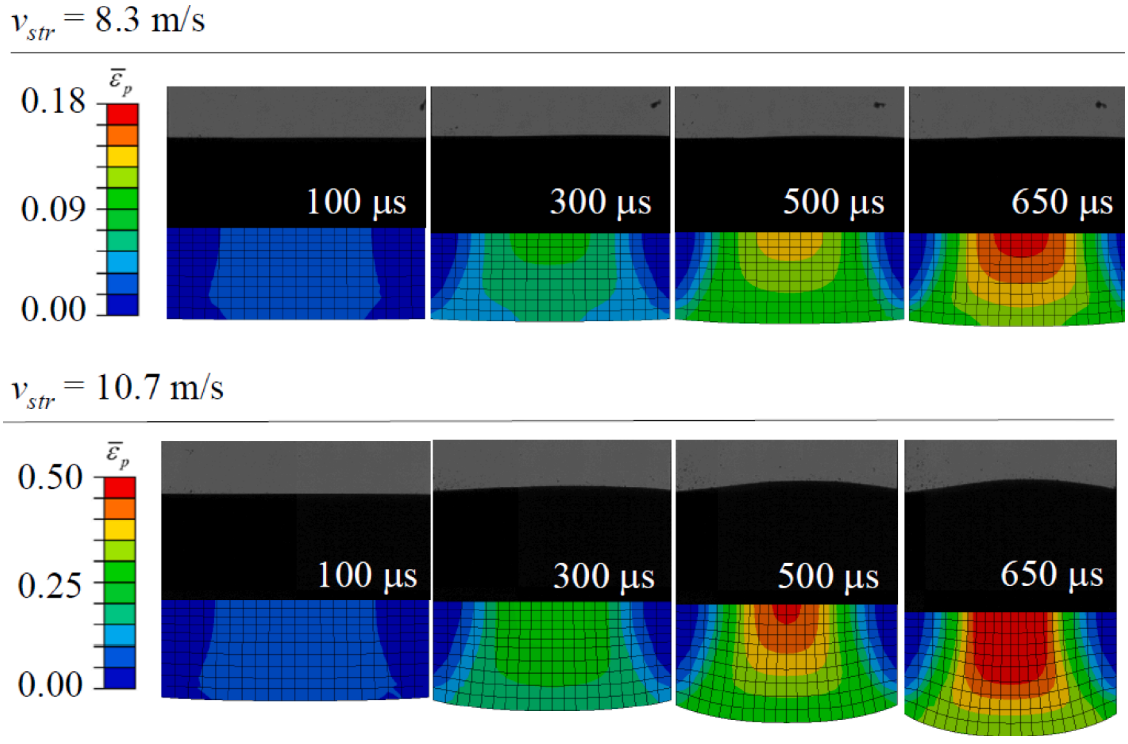

Fig. 12. Comparison between the experimental and numerical profiles of the compression specimens with striker velocities of 8.3(top) and 10.7 (bottom) m/s.

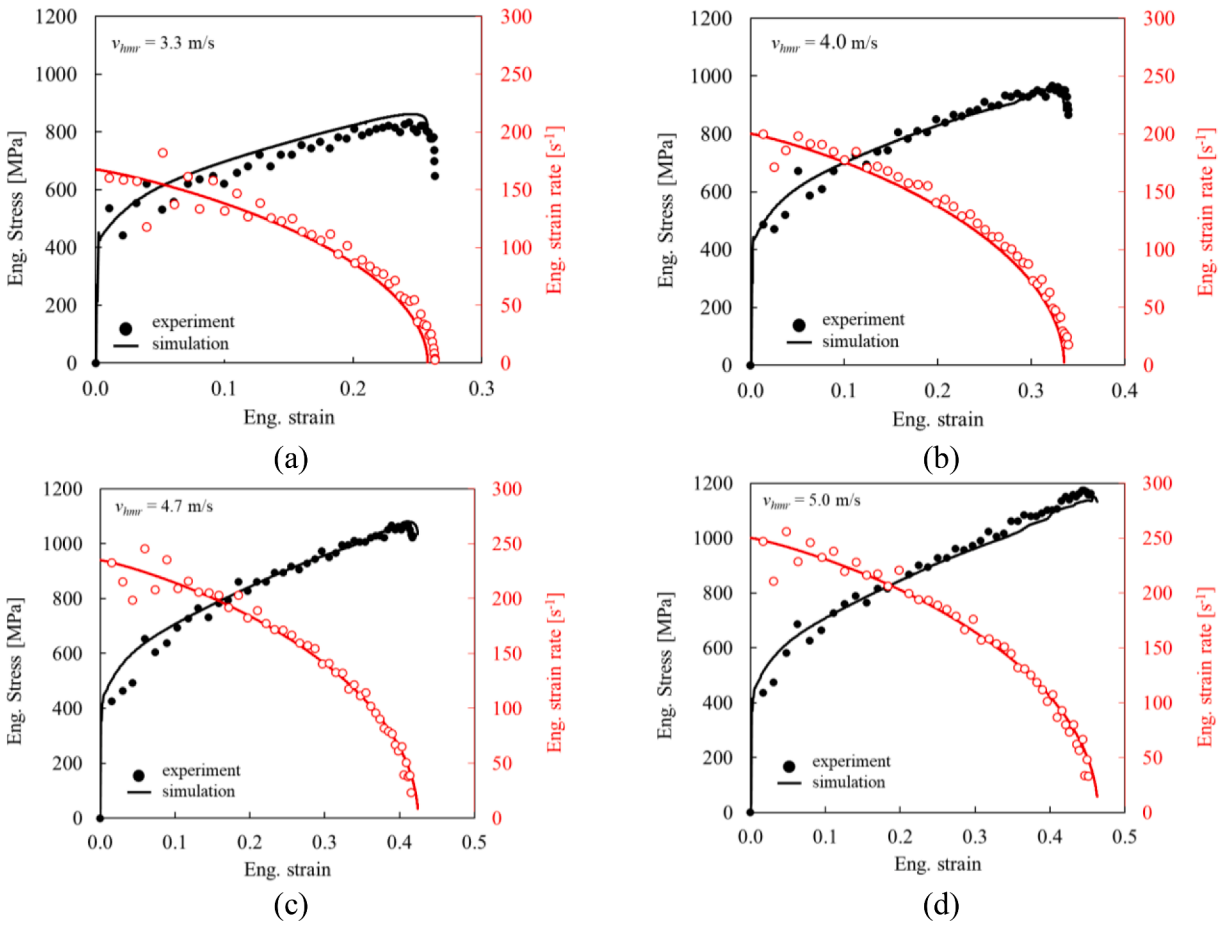

Fig. 13. Engineering stress-strain and strain rate-strain numerical responses compared with the experiments with hammer velocities of 3.3m /s (a), 4m /s (b), 4.7m /s (c), and 5m /s(d).

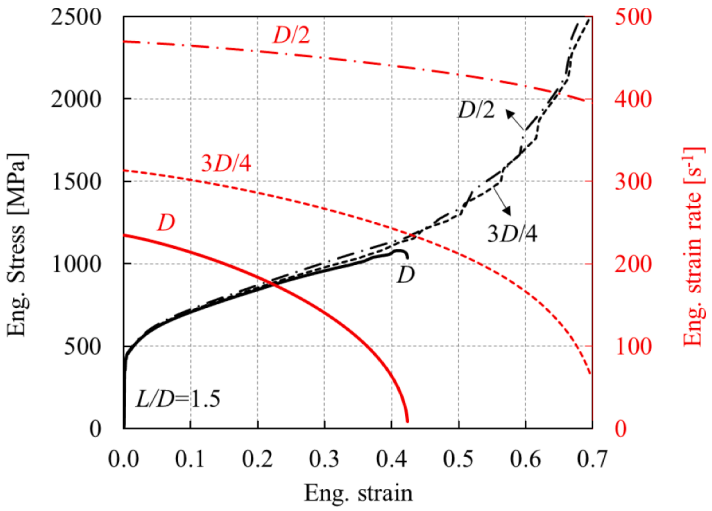

Fig. 14. Specimen size effect on the numerical engineering stress-strain and strain rate-strain response.

strains up to 0.15. The smaller m value in the cal. SHPB however, corrected that effect as the strains increased and the stress levels from the two calibrations seemed to converge, at least for the strain ranges that were studied. The larger scatter in the DIDH tests at the beginning of the stress-strain curves forced the optimisation software employed in the inverse modelling procedure to lift it up by increasing the C constant, which as a consequence increased m to fit the stress level for larger strains. Comparatively, for the range of strains analysed, there are only slight differences amongst the two calibrations. More importantly, the numerical simulations of the SHPB tests with the cal. HMR were in very good agreement with the experimental data which reinforced the idea of using the DIDH tests as calibration tests for the intermediate strain rate regime.

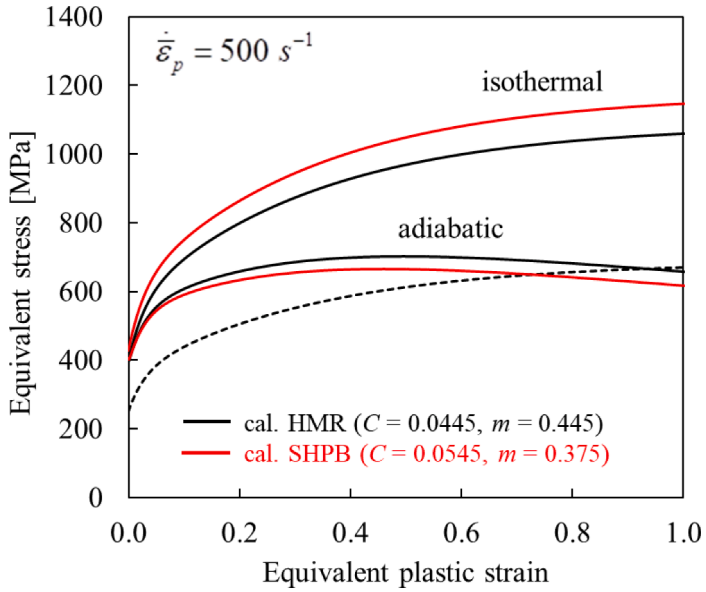

Fig. 15. Adiabatic and isothermal equivalent stress-plastic strain curves given by the Johnson-Cook strength model calibrated with the SHPB and DIDH tests for a constant equivalent plastic strain rates of 500 s^{-1}.

6.3. Full-scale DIDH simulations

Although excellent agreement was obtained between experimental and numerical mechanical responses, as shown in the previous subsection, there were still certain experimentally-observed effects such as the initial oscillations that were not captured in the simplified simulations. To study this in detail, half of the DIDH was modelled making use of its horizontal symmetry condition as shown in Fig. 17. The parts that comprised the model are depicted in Fig. 17. All contacts except for the specimen-anvil and specimen-hammer interfaces were modelled as frictionless. All the grey parts in Fig. 17, this is the hammer and the rig, and the anvil were considered isotropic elastic with the same properties as the S235JR steel. For the sake of simplicity, the load sensor was considered as an orthotropic elastic material (see Table 5) with no piezoelectric effect following Hooke's law, $\boldsymbol{\sigma} = \mathbb{C}^{oR} : \boldsymbol{\varepsilon}$, where $\mathbb{C}^{oR}$ contains the elastic constants reported in [19] and in matrix form has the shape:

$$\left[\mathbb{C}^{oR}\right] = \begin{bmatrix} c_{11} & c_{12} & c_{13} & 0 & 0 & 0 \\ & c_{11} & c_{13} & 0 & 0 & 0 \\ & & c_{33} & 0 & 0 & 0 \\ & sym & & c_{44} & 0 & 0 \\ & & & & c_{44} & 0 \\ & & & & & c_{44} \end{bmatrix} \tag{12}$$

The hyperelastic behaviour of the rubber pad on the bottom of the rig was described by a three-term Ogden model with the following strain energy density U expression in terms of the principal stretches, $\lambda_I, \lambda_{II}, \lambda_{III}$,

$$U[\lambda_I, \lambda_{II}, \lambda_{III},] = \sum_{i=1}^{3} \frac{\mu_i}{2\alpha_i^2}\left(\lambda_I^{'\alpha_i} + \lambda_{II}^{'\alpha_i} + \lambda_{III}^{'\alpha_i} - 3\right) + \sum_{i=1}^{3} \frac{1}{D_i}(\det[F] - 1)^{2i} \tag{13}$$

where $\lambda_i^{'} = \mathrm{dev}[\lambda_i] = \lambda_i(\det[\mathbf{F}])^{-1/3}$ for $i = I, II, III$ and the material constants as detailed in [5] calibrated from [37] and reported in Table 5.

The element size used to discretise the specimen was maintained equal to that in previous sections, but it was coarsened for the rest of the parts. It should be noted that for the sake of simplicity, no connectors such as bolts or screws were modelled. However, the dimensions, geometries and weights of the complete assembly were respected as much as possible. The DIDH experiment conducted at 4.7 m/s was simulated, where contact force measurements from the specimen-anvil, specimen-hammer and anvil-load sensor interfaces were extracted. The force extracted from the specimen interfaces, as shown in Fig. 18(a), were almost identical from the beginning, with differences below 1% of the maximum force for most of the duration of the test. Therefore, the oscillations observed in the experimental stress-strain curves (see Fig. 6) have an origin that is not related to the dynamic force equilibrium. This is in accordance with the discussion in Section 4.2, where calculating the time that the stress waves took to complete five round trips, we hypothesised that the specimen was in equilibrium

Fig. 18(b) compares the experimental force history (in grey) against the contact force read from the anvil-load cell sensor interface (in red), where the same oscillatory behaviour was detected. Several authors that employed similar load cell arrangements such as [27,25,47] have come across comparable effects concluding that the system ringing [15] is responsible for the oscillations in the load measurements. The impulse generated by the system during the test can excite the relatively low natural frequency of the piezoelectric load sensor causing spurious oscillations in the load signal. These oscillations increase with larger applied velocities as the stress wave amplitude increases.

6.4. System ringing analysis

The system ringing is typically analysed with a simplified single degree of freedom (SDOF) mass-spring-damper analysis such as that shown in Fig. 19, where the force history measured from the specimen-anvil interface $F[t]$ is used as an input. Such a force acts on a mass m_1 that represents the anvil which is connected to the rig assembly with a spring of stiffness k_1 and a damper with a viscous coefficient c_1 that simulate the load sensor. The viscous damping coefficient is typically defined through the relation $c_1 = \zeta_1\sqrt{4k_1m_1}$ being ζ_1 the damping ratio, a dimensionless parameter. The stiffness was approximated as $k_1 = A_1E_1/L_1$, where $L_1 = 15\text{mm}$ is the length and $A_1 = 1589\text{mm}^2$ is the cross-section area of the load sensor. For detailed information on the dimensions the reader is referred to the manufacturer's product data sheet. Due to its large mass concentrated close to the impact zone, the rig's top plate, shown in the detail of Fig. 17, has been considered as an element with mass m_2 connected to the floor with a large steel column that is considered to be very, which is treated as a spring of stiffness k_2. The measured mass of the anvil is $m_1 = 1.54kg$ and the approximated mass of the top plate is $m_2 = 47kg$.

The "real" force that the specimen was subjected to, acted on the system deforming elastically the load sensor which in turn, through the

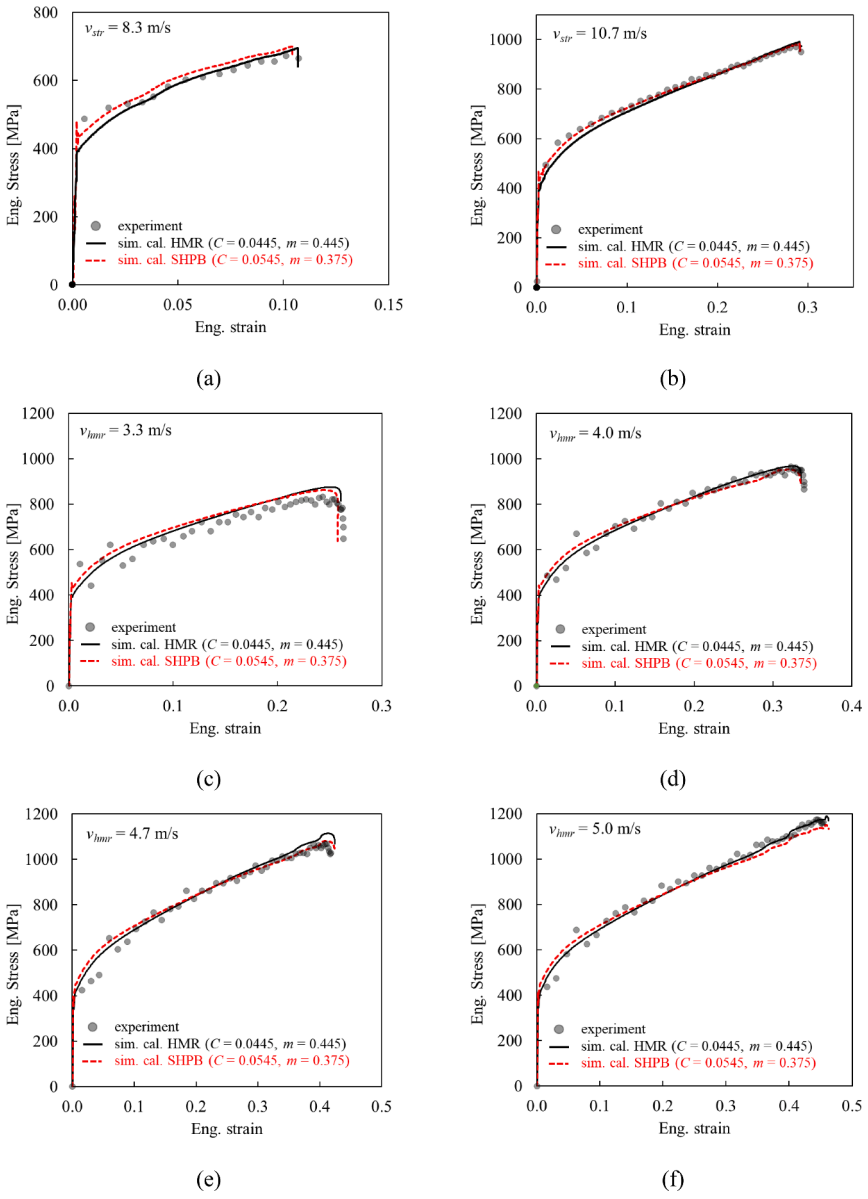

Fig. 16. Comparison of the numerical engineering stress-strain responses from the simulations performed with a set of constants calibrated with the SHPB tests and another set calibrated with the DIDH tests.

piezoelectric effect, gave the force signal. Although we knew of the orthotropic behaviour of the sensor, for this particular case we assumed that has an isotropic elastic modulus of $E_1 = 126$GPa. The output force $F_{\text{SDOF}}[t]$, depicted in blue in Fig. 19, represents the load signal "contaminated" by the ringing effect and it can be calculated employing Hooke's law as:

$$F_{\text{SDOF}}[t] = k_1(x_1[t] - x_2[t]) \tag{14}$$

where $x_1[t]$ and $x_2[t]$ are the displacements calculated solving the following set of ordinary differential equations:

$$\begin{aligned} m_1\ddot{x}_1[t] + c_1(\dot{x}_1[t] - \dot{x}_2[t]) + k_1(x_1[t] - x_2[t]) - F_{\text{spec-anvil}}[t] = 0 \\ m_2\ddot{x}_2[t] - c_1(\dot{x}_1[t] - \dot{x}_2[t]) - k_1(x_1[t] - x_2[t]) + k_2x_2[t] = 0 \end{aligned} \tag{15}$$

with the initial conditions $x_i[t] = \dot{x}_i[t] = 0$ for $i = 1, 2$.

The complex geometry of the column that connects the upper part of the DIDH with the floor is far more complex than what is depicted in Fig. 17, which makes the stiffness k_2 estimation quite challenging. It has been obtained choosing a viscous damping ratio of $\zeta_1 = 0.07$ and minimising the following error function:

$$f_{error} = \sqrt{\frac{\sum_{t=0}^{T}\left(F_{\text{SDOF}}[t] - F_{\text{exp}}[t]\right)^2}{T}} \tag{16}$$

The resulting response for different viscous damping ratios is plotted and compared against the experimental data in Fig. 20 and against the simulation in Fig. 18(b). The resulting natural frequencies of this analysis calculated as:

$$f_{0,i} = \frac{1}{2\pi}\sqrt{\frac{k_i}{m_i}} \tag{17}$$

are $f_{01} = 14.5$kHz and $f_{01} = 2.6$kHz. On the one hand, it seemed that the lowest frequency did not masque excessively the experimental results, but it was always excited. On the other hand, although the highest has a significant effect, it was quickly attenuated in comparison with the total test time.

It should be noted that the SDOF analysis is far too simplistic to

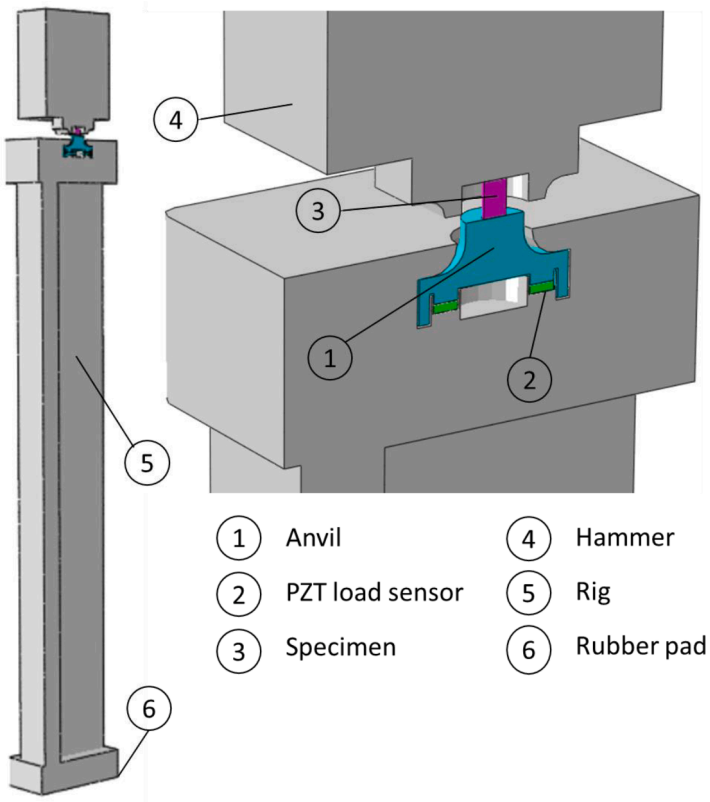

Fig. 17. Schematic view of the full-scale DIDH assembly.

Table 5
Material properties of the load sensor from [19] and rubber pad from [5].

Load sensor							
ρ[kg /m^3]	μ_1[MPa]	α_1	μ_2[MPa]	α_2	μ_3[MPa]	α_3	D_i[MPa^{-1}]
7500	0.00183	5.305	0.00911	-2.066	0.39	1.432	0.001
Rubber pad							
ρ[kg /m^3]	c_{11}[GPa]	c_{33}[GPa]	c_{12}[GPa]	c_{13}[GPa]	c_{44}[GPa]		
1400	126	117	79.5	84.1	23.5		

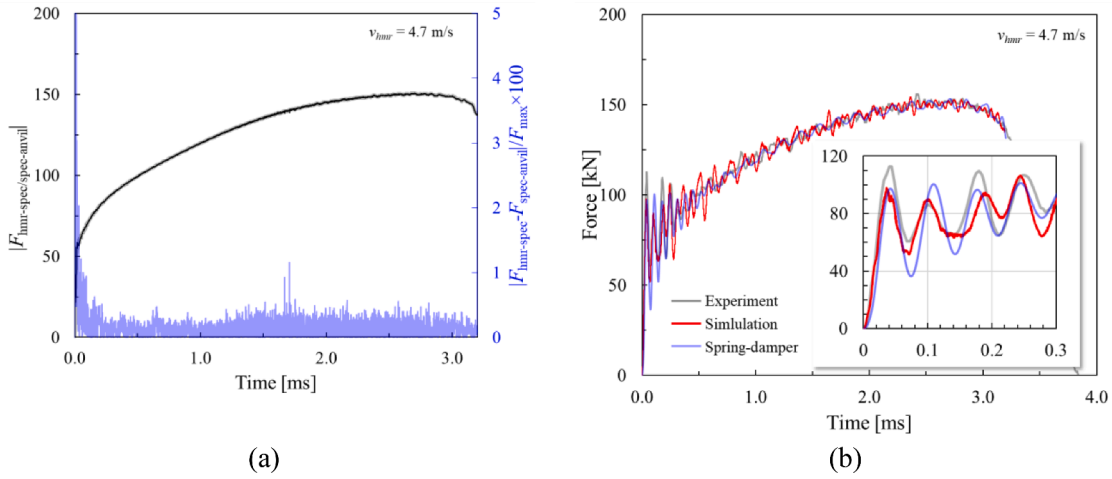

Fig. 18. (a) Force signal extracted from the hammer-specimen and anvil-specimen interfaces (in black) and the relative force difference between both interfaces (in blue). (b) Experimental and anvil-load cell interface simulation contact force histories.

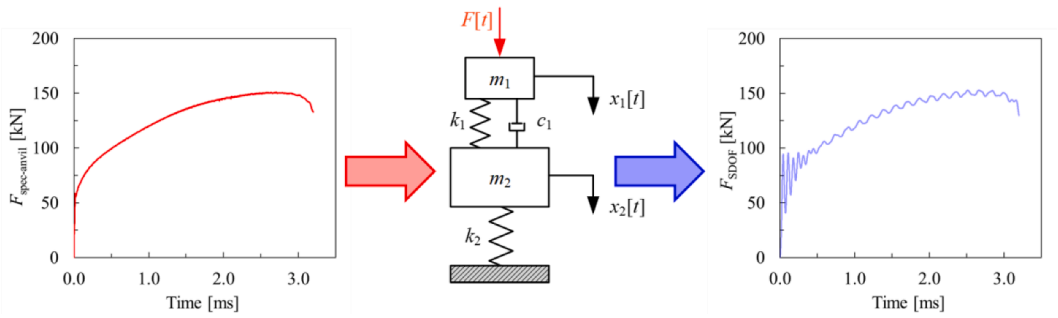

Fig. 19. Schematical representation of the system ringing represented by a simplified single degree of freedom mass-spring-damper system.

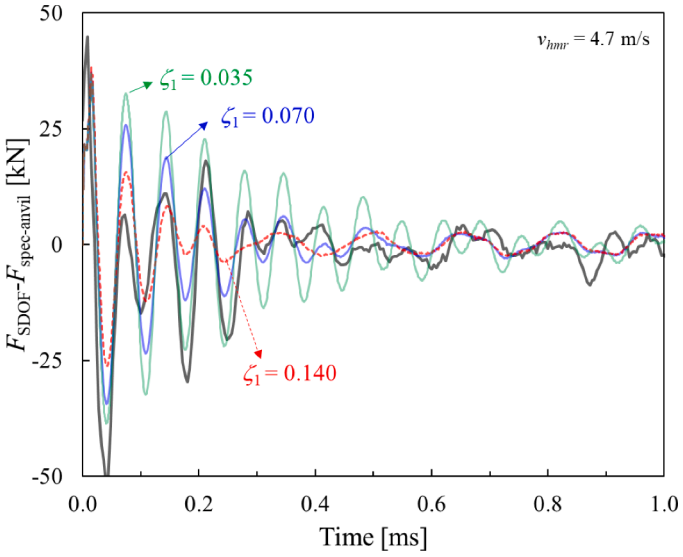

Fig. 20. Experimental force measurement for a test at 4.7 m/s hammer velocity in the DIDH (black) against SDOF analysis results for different viscous damping ratios.

capture all the details of the testing apparatus. However, it seems to give some trends, and most importantly, can give an assessment on the amount of the system's ringing effect on the experimental load signal.

7. Conclusions

Given the limitations of conventional mechanical testing apparatuses to test at intermediate strain rates, a Direct Impact Drop Hammer (DIDH) that can be employed as a mechanical testing device for tests at such strain rate range and at both room temperature and high temperatures (<1000 °C) has been designed and developed. It is a testing module of the larger and more ambitious Automatic Thermo-Mechanical Tester (ATMT) focused on metal forming operations. The design details, the functioning principles and the equipment that provided force and displacement measurements have been presented. Despite its disadvantages, such as the limited hammer kinetic energy or the inability to track the real time specimen deformation, it has been shown that is capable of accurately and repetitively test under compressive loads at intermediate strain rates and both room and high temperatures. The DIDH allowed testing at average strain rates in the order of 100 s^{-1} that decrease progressively as its energy was converted into specimen's deformation energy until it was fully stopped. We have shown that in combination with universal testing machines and Hopkinson bar systems, is a device that is very well suited for the experimental validation of loading-rate dependant computational material models.

There is definitely room for improvement, since the machine is still in its early stages of development. A transparent shield that would allow directly recording the specimen deformation throughout the straining process is already being implemented. Other technical aspects such faster image acquisition or interchangeable hammer heads would also improve some of the issues that have been pointed out.

To test the capabilities of the DIDH, compression experiments on S235JR low-alloy steel have been performed in both the DIDH and a SHPB. The results highlighted some of the limitations of the SHPB when it comes to the intermediate strain rate testing. In particular, the pulse generated by the striker has not been large enough to sufficiently compress the specimens to a degree that would allow a direct comparison with the DIDH tests at similar strain rates. Conversely, the DIDH tests at several loading rates have showed the possibilities of the newly constructed apparatus. Although the strain rate decreased as the specimens were strained, it has not been considered as a drawback, but simply an effect of the specimen size. Additionally, room temperature tests on OFHC copper samples at various intermediate strain rates, and high temperature (950–1150 °C) tests on Inconel 625 nickel-based superalloy samples have been performed in the DIDH. The results showed a high repeatability showcasing the capabilities of the DIDH as an experimental device to characterise materials' behaviour at both intermediate strain rates and high temperatures.

To further asses the suitability of the newly developed DIDH for intermediate strain rate testing, the S235JR steel has been calibrated for an associative von Mises plasticity with a Johnson-Cook-type hardening law, with some additional quasi-static tensile and compression tests and the SHPB experiments. The calibrated material model has been used to run FE simulations with simple boundary conditions of the DIDH tests showing an excellent agreement with the experimental mechanical responses. To show the potential that the DIDH tests have as a set of data in the intermediate strain rate regime to calibrate computational models for metal forming applications and to add another layer of confidence, the Johnson-Cook constants that control the loading rate behaviour have been recalibrated with such tests. This new calibration has been compared against the previous exhibiting minor differences in the numerical stress-strain responses of the SHPB and DIDH tests reinforcing the possibility of using the DIDH experiments as material calibration data in the intermediate strain rate regime. Additionally, the FE models with smaller specimen sizes have been simulated showing the influence of their geometry for the same DIDH setup. Finally, the source of the experimental force oscillations has been analysed with a full-scale DIDH FE model in a simulation study, concluding that such an oscillation does not have its origin in the lack of the dynamic equilibrium but in the system's ringing produced by the excitation of the piezoelectric force sensor's natural frequency after hammer impact.

CRediT authorship contribution statement

Julen Agirre: Conceptualization, Methodology, Formal analysis, Writing – original draft, Investigation. **David Abedul:** Methodology, Formal analysis, Investigation. **Eneko Saenz de Argandoña:** Writing –

review & editing, Resources. **Nagore Otegi:** Funding acquisition, Project administration, Writing – review & editing. **Lander Galdos:** Methodology, Funding acquisition, Project administration, Writing – review & editing. **Borja Erice:** Investigation, Software, Writing – original draft, Writing – review & editing, Supervision.

Declaration of Competing Interest

The authors declare the following financial interests/personal relationships which may be considered as potential competing interests: Borja Erice reports financial support was provided by Spain Ministry of Science and Innovation. Julen Agirre reports financial support was provided by Basque Government. Borja Erice reports financial support was provided by Research Council of Norway.

Data availability

Data will be made available on request.

Acknowledgments

The authors would like to thank the Basque Government for the financial support given through the research projects OGFORGE (Hazitek ZL-2019/00161), DIGICUT (Elkartek KK-2019/00071) and TUBALLOY (Elkartek KK-2018/00061). Special thanks to ULMA Forja S. Coop., Fagor Arrasate S. Coop. and Tubacex S.A. for partially sponsoring this investigation. The authors would also like to thank the Centre for Advanced Structural Analysis (CASA) (Project No. 237885 funded by the Research Council of Norway) at the Norwegian University of Science and Technology (NTNU). Special thanks also to Mr. Trond Auestad for his assistance with the SHPB experiments. The author Borja Erice would like to acknowledge the support from the Grant RYC2021-033241-I funded by MCIN/AEI/ 10.13039/501100011033 and by "European Union NextGenerationEU/PRTR".

Supplementary materials

Supplementary material associated with this article can be found, in the online version, at doi:10.1016/j.ijimpeng.2023.104764.

References

[1] ABAQUS/explicit user's manual, version 6.14. United States: Dassault Systèmes Simulia Corp; 2014.
[2] Agirre J. Development of a thermomechanical tester for intermediate strain rates and phenomenological modelling of microstructural evolution: application to hot forging of inconel 625. Mondragon Unibertsitatea; 2022.
[3] Altan T, Ngaile G. ASM cold and hot forging. ASM International; 2005.
[4] Bardenheier R, Rogers G. Dynamic impact testing with servohydraulic testing machines. J Phys 2006;134:693–9. IV : JP.
[5] Bergström J. Mechanics of solid polymers. Elsevier; 2015.
[6] Bhujangrao T, Froustey C, Iriondo E, Veiga F, Darnis P, Mata FG. Review of intermediate strain rate testing devices. Metals 2020;10:1–24 (Basel).
[7] Bussac MN, Collet P, Gary G, Othman R. An optimisation method for separating and rebuilding one-dimensional dispersive waves from multi-point measurements. Application to elastic or viscoelastic bars. J Mech Phys Solids 2002;50:321–49.
[8] Chen XM, Lin YC, Chen MS, Li HB, Wen DX, Zhang JL, He M. Microstructural evolution of a nickel-based superalloy during hot deformation. Mater Des 2015;77:41–9.
[9] Dieter GE, Kuhn HA, Semiatin SL. Handbook of workability and process design. ASM International; 2003.
[10] Follansbee PS, Kocks UF. A constitutive description of the deformation of copper based on the use of the mechanical threshold stress as an internal state variable. Acta Metall 1988;36:81–93.
[11] Froustey C, Lambert M, Charles JL, Lataillade JL. Design of an impact loading machine based on a flywheel device: application to the fatigue resistance of the high rate pre-straining sensitivity of aluminium alloys. Exp Mech 2007;47:709–21.
[12] Gary G, Mohr D. Modified kolsky formulas for an increased measurement duration of SHPB systems. Exp Mech 2013;53:713–7.
[13] GOM. GOM Correlate pro user's manual. GOM; 2019.
[14] Gray GT. Classic split-Hopkinson pressure bar testing. Mech Test Eval 2000.
[15] House JW, Gillis PP. Testing machines and strain sensors. Mech Test Eval 2000:79–92.
[16] Jaspers SPFC, Dautzenberg JH. Material behaviour in metal cutting: strains, strain rates and temperatures in chip formation. J Mater Process Technol 2002;121:123–35.
[17] Jia B, Rusinek A, Pesci R, Bernier R, Bahi S, Bendarma A, Wood P. Simple shear behavior and constitutive modeling of 304 stainless steel over a wide range of strain rates and temperatures. Int J Impact Eng 2021:103896.
[18] Johnson GR, Cook WH. A constitutive model and data for metals subjected to large strains, high strain rates and high temperatures. In: Proceedings of the 7th International Symposium on Ballistics; 1983. p. 541–7.
[19] Kunkel HA, Locke S, Pikeroen B. Finite-element analysis of vibrational modes in piezoelectric ceramic disks. IEEE Trans Ultrason Ferroelectr Freq Control 1990;37:316–28.
[20] LeBlanc MM, Lassila DH. A hybrid technique for compression testing at intermediate strain rates. Exp Tech 1996;20:21–4.
[21] LS-OPT user's manual. United States: Livermore Software Technology Corporation; 2019.
[22] Lundberg B, Henchoz A. Analysis of elastic waves from two-point strain measurement. Exp Mech 1977;17:213–8.
[23] Nicolaÿ A, Fiorucci G, Franchet JM, Cormier J, Bozzolo N. Influence of strain rate on subsolvus dynamic and post-dynamic recrystallization kinetics of Inconel 718. Acta Mater 2019;174:406–17.
[24] Othman R, Gary G. Testing aluminum alloy from quasi-static to dynamic strain-rates with a modified Split Hopkinson Bar method. Exp Mech 2007;47:295–9.
[25] Perogamvros N, Mitropoulos T, Lampeas G. Drop tower adaptation for medium strain rate tensile testing. Exp Mech 2016;56:419–36.
[26] Prasad YVRK, Rao KP, Sasidhara S. Hot working guide - a compendium of processing maps. 2nd ed. Mater Eng 2015.
[27] Qin Z, Zhu J, Li W, Xia Y, Zhou Q. System ringing in impact test triggered by upper-and-lower yield points of materials. Int J Impact Eng 2017;108:295–302.
[28] Quinlan MF, Hillery MT. High-strain-rate testing of beryllium copper at elevated temperatures. J Mater Process Technol 2004;153–154:1051–7.
[29] Semiatin SL. ASM handbook: metalworking: bulk forming. ASM International; 2005.
[30] Senkov ON, Jonas JJ. Effect of strain rate and temperature on the flow stress of β-phase titanium-hydrogen alloys. Metall Mater Trans A Phys Metall Mater Sci 1996;27:1303–12.
[31] Shim J, Mohr D. Using split Hopkinson pressure bars to perform large strain compression tests on polyurea at low, intermediate and high strain rates. Int J Impact Eng 2009;36:1116–27.
[32] Song B, Chen WW, Lu WY. Mechanical characterization at intermediate strain rates for rate effects on an epoxy syntactic foam. Int J Mech Sci 2007;49:1336–43.
[33] Song B, Sanborn B, Heister J, Everett R, Martinez T, Groves G, Johnson E, Kenney D, Knight M, Spletzer M. Development of "dropkinson" Bar for intermediate strain-rate testing. In: Proceedings of the EPJ Web of Conferences. 183; 2018. p. 1–6.
[34] Song B, Syn CJ, Grupido CL, Chen W, Lu WY. A long split Hopkinson pressure bar (LSHPB) for intermediate-rate characterization of soft materials. Exp Mech 2008;48:809–15.
[35] Srivatsan TS, Hoff T, Sriram S, Prakash A. The effect of strain rate on flow stress, strength and ductility of an Al-Li-Mg alloy. J Mater Sci Lett 1990;9:297–300.
[36] Tan YB, Ma YH, Zhao F. Hot deformation behavior and constitutive modeling of fine grained Inconel 718 superalloy. J Alloy Compd 2018;741:85–96.
[37] Treloar, L., 1975. The physics of rubber elasticity.
[38] Tulke M, Scheffler C, Psyk V, Landgrebe D, Brosius A. Principle and setup for characterization of material parameters for high speed forming and cutting. Procedia Eng 2017;207:2000–5.
[39] Vazquez-Fernandez NI, Soares GC, Smith JL, Seidt JD, Isakov M, Gilat A, Kuokkala VT, Hokka M. Adiabatic heating of austenitic stainless steels at different strain rates. J Dyn Behav Mater 2019;5:221–9.
[40] Viot P. Hydrostatic compression on polypropylene foam. Int J Impact Eng 2009;36:975–89.
[41] Whittington WR, Oppedal AL, Francis DK, Horstemeyer MF. A novel intermediate strain rate testing device: the serpentine transmitted bar. Int J Impact Eng 2015;81:1–7.
[42] Xu D, Zhang W, Yu L, Xin X, Qi F, Sun W, Jia D. Abnormal dynamic recrystallization behavior of a nickel based superalloy during hot deformation. J Alloy Compd 2019.
[43] Yamada H, Kami T, Mori R, Kudo T, Okada M. Strain rate dependence of material strength in aa5xxx series aluminum alloys and evaluation of their constitutive equation. Metals 2018;8:1–15 (Basel).
[44] Yoshino M, Shirakashi T. Flow-stress equation including effects of strain-rate and temperature history. Int J Mech Sci 1997;39:1345–62.
[45] Zaretsky EB, Kanel GI. Effect of temperature, strain, and strain rate on the flow stress of aluminum under shock-wave compression. J Appl Phys 2012;112:1–9.
[46] Zhang H, Zhang K, Zhou H, Lu Z, Zhao C, Yang X. Effect of strain rate on microstructure evolution of a nickel-based superalloy during hot deformation. Mater Des 2015;80:51–62.
[47] Zhu D, Rajan SD, Mobasher B, Peled A, Mignolet M. Modal analysis of a servo-hydraulic high speed machine and its application to dynamic tensile testing at an intermediate strain rate. Exp Mech 2011;51:1347–63.
[48] Zhu X, Liu D, Xing LJ, Hu Y, Yang YH. Microstructure evolution of inconel 718 alloy during ring rolling process. Int J Precis Eng Manuf 2016;17:775–83.